International Journal of Biological Macromolecules 253 (2023) 127088

Contents lists available at ScienceDirect

International Journal of Biological Macromolecules

journal homepage: www.elsevier.com/locate/ijbiomac

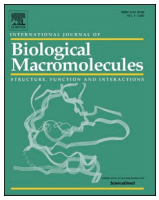

Assessing the interaction between hemoglobin and the receptor binding domain of SARS-CoV-2 spike protein through MARTINI coarse-grained molecular dynamics

Jessica Gasparello [a,1], Marco Verona [b,1], Adriana Chilin [b], Roberto Gambari [a], Giovanni Marzaro [b,*]

[a] Department of Life Sciences and Biotechnology, University of Ferrara, via Fossato di Mortara 74, 44121 Ferrara, Italy
[b] Department of Pharmaceutical and Pharmacological Sciences, University of Padova, via Marzolo 5, 35313 Padova, Italy

ARTICLE INFO

Keywords:
SARS-CoV-2
Hemoglobin
Spike-protein
Molecular dynamics
Metadynamics

ABSTRACT

The emergence of different coronavirus-related diseases in the 2000's (SARS, MERS, and Covid-19) warrants the need of a complete understanding of the pathological, biological, and biochemical behavior of this class of pathogens. Great attention has been paid to the SARS-CoV-2 Spike protein, and its interaction with the human ACE2 has been thoroughly investigated. Recent findings suggested that the SARS-CoV-2 components may interact with different human proteins, and hemoglobin has very recently been demonstrated as a potential target for the Spike protein. Here we have investigated the interaction between either adult or fetal hemoglobin and the receptor binding domain of the Spike protein at molecular level through advanced molecular dynamics techniques and proposed rational binding modes and energy estimations. Our results agree with biochemical data previously reported in literature. We also demonstrated that co-incubation of pulmonary epithelial cells with hemoglobin strongly reduces the pro-inflammatory effects exerted by the concomitant administration of Spike protein.

1. Introduction

Since its appearance in late 2019, the SARS-CoV-2 has caused about seven million deaths, according to the World Health Organization (WHO). This new member of the coronavirus family caused the Covid-19 pandemic [1]. Unprecedent efforts have been made to repurpose known drugs and to promptly develop new vaccines to furnish effective pharmacological tools against the Covid-19 [2,3]. Although very recently the international Covid-19 emergency was declared over by the WHO, the occurrence of the long-Covid syndrome [4] as well as the recurring rise of coronavirus-related diseases (SARS-CoV in 2003 and MERS-CoV in 2012) are necessitating the full comprehension of the pathological, biological, and biochemical behavior of this class of pathogens. In this view, the structures of most SARS-CoV-2 components have been characterized by means of both crystallographic, cryo-EM, and molecular dynamics experiments, shedding the light on the mechanism of invasion and replication [5]. Particular attention has been paid to the Spike (S) protein, that is responsible for the host-cell recognition through the binding between its Receptor Binding Domain (RBD) and the human type-2 Angiotensin Converting Enzyme (ACE2). Indeed, the RBD/ACE2 binding was clearly demonstrated as the triggering event for the infection of pulmonary epithelial cells [6]. The S-protein has also been the main target for the development of the vaccines [3], and the mutants emerged during the pandemic has been used to classify the different variants characterized by different lethality and infectivity [7]. The SARS-CoV-2 infects different human organs, and the tissue expression of the ACE2 only partially justify the virus tropism, suggesting that the S-protein may interact with a variety of other host proteins [8,9]. Of note, isolated S-protein showed toxic effects on cells [10,11], further confirming that the S-protein interaction with other human proteins can alter their physiological functions. In this view, the dramatic effects of SARS-CoV-2 on the behavior of red blood cells and human adult hemoglobin (HbA) physiology have been reported [12]. Reduced levels of HbA in patients have also been recognized by several authors as a predictive marker for severity and increased risk of mortality in Covid-19 patients [13–15].

* Corresponding author.
E-mail address: giovanni.marzaro@unipd.it (G. Marzaro).
[1] Contributed equally to the work and must be considered as co-first authors.

https://doi.org/10.1016/j.ijbiomac.2023.127088
Received 10 July 2023; Received in revised form 22 September 2023; Accepted 24 September 2023
Available online 27 September 2023

HbA is a well-characterized protein, responsible for the delivery of molecular oxygen to and for the removal of carbon dioxide from the tissues. From a structural point of view, HbA is a hetero-tetrameric globular protein of ellipsoidal shape. HbA shows $\alpha_2\beta_2$ quaternary structure, with each sub-unity containing one heme cofactor responsible for the O_2/CO_2 transport ability [16]. HbA shows at least two energetic favorable states, named "T" (tense, O_2/CO_2 unbound) and "R" (relaxed, O_2/CO_2 bound). T- and R-states differ from the interactions between α_n and β_m chain, whereas the interactions between α_n and β_n chains are almost maintained [17]. A schematic representation of HbA is reported in Fig. 1.

During the development of the organism, the production of hemoglobin switches from the fetal (HbF) to the adult HbA form [18]. HbF differs from HbA in that the former is an $\alpha_2\gamma_2$ tetramer, i.e., HbF and HbA share only the α-subunits. HbF is known to possess higher affinity than HbA for O_2, allowing the fetus to "extract" the oxygen from the mother's blood [19]. HbF is poorly expressed in normal adults and has a negligible physiological effect. However, HbF plays an important role in β-thalassemia, a rare genetic condition characterized by reduced or absent synthesis of hemoglobin β-chains, leading to poor or null production of HbA and thus severe blood dysfunctions [20]. Of note, some β-thalassemia patients show increased production of HbF, that ameliorates their clinical conditions [21]; furthermore, it has been reported that induction of HbF production can be an effective pharmacological strategy [22].

In 2021, Lechuga et al. [23] proposed that different SARS-CoV-2 proteins, including the S-protein, can bind HbA, showing that pre-incubation of Vero E6 cells with HbA reduced both virus infection and replication. Biochemical experiments using short peptides with sequences derived from different regions of the S-protein suggested the RBD as the most probable site of binding for HbA [23]. Later on, Dyankov et al. further demonstrated that HbA binds to RBD by means of Surface Plasmonic Resonance (SPR) experiments [24]. Additionally, we have recently found that induction of S-protein expression in erythroid cells affects hemoglobin accumulation [R. Gambari, submitted paper]. Taken together, these data support the hypothesis that hemoglobin can be an effective target for S-protein and that this protein interaction deserves further exploration. The exact binding mode between RBD and HbA remains elusive. Indeed, different computational tools have been used to predict the RBD-HbA interaction, thus leading to quite different binding geometries [23]. A more exhaustive prediction of RBD/HbA and RBD/HbF interactions could be obtained employing molecular dynamics (MDs) [25] rather than protein docking simulations, of course at higher costs in terms of computational time. Several techniques to enhance the sampling in MDs have been developed with the aim of reducing the very long time required to study a specific molecular event [26]. Among them, Well-Tempered MetaDynamics (WTMDs) was proven to furnish a reliable estimation of the Free Energy Surface (FES) for a given specific molecular system as a function of few degrees of freedom (named collective variables; CVs), i.e., descriptors of the molecular system able to distinguish between the different states that can be visited [27]. In WTMDs, a history dependent bias potential is added throughout the simulation enhancing the sampling of the different values that can be assumed by the CVs, and the height of the added potential is progressively reduced thus facilitating the energy convergence [27]. The FES, as function of the CVs, is then reconstructed by applying a reweighting scheme [28]. The choice of the most appropriate CVs is not trivial and depends on the event (e.g.: binding/unbind process; intermolecular interaction; protein rearrangement; folding/unfolding process; etc.) under investigation. In principle, WTMDs can be used to study the RBD-HbA(HbF) interactions in terms of both geometry and energy, provided that a set of CVs can be identified that distinguish between the bound and unbound states. This, however, would require including the proteins in a simulation box large enough to guarantee that, even in the unbound state, the periodic images are not interacting with each other and microseconds of simulations. Despite the availability of sampling enhancing techniques, studying such large molecular systems for such a long time requires dedicated hardware with high

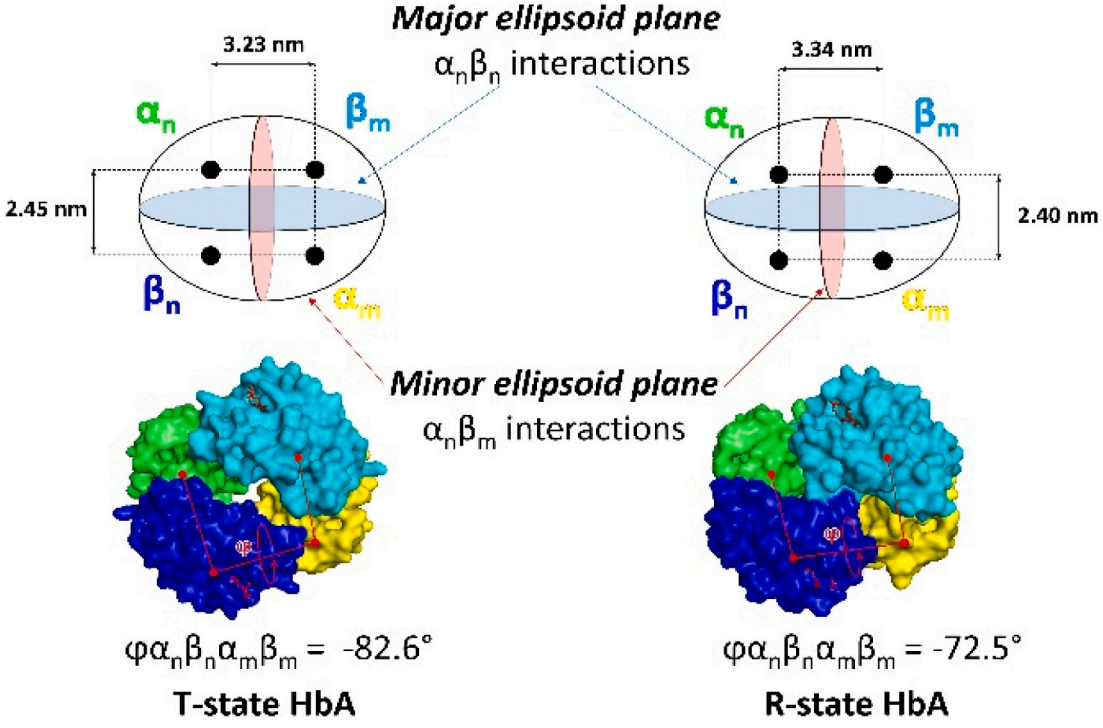

Fig. 1. Schematic (top) and surface (bottom) representation of human adult hemoglobin (HbA). Left: T-state HbA; right: R-state HbA. Black dots represent the geometrical centroids of each subunit, determined as the center of mass of Cα-atoms. T-state structure was derived from PDB-ID: 2hhb. R-state structure was derived from PDB-ID: 1bbb.

computing performance. A powerful strategy to reduce the computational cost of large systems is the use of coarse-grained (CG) approximation in which groups of atoms are joined into "beads" [29]. Different CG force fields have been developed so far. Among them, the MARTINI force field proved the ability to depict both the geometry and the energy of inter- and intra-molecular interactions with remarkable agreement with all-atoms simulations [29–31]. In MARTINI, each amino acid is represented by one backbone (BB) bead and additional 0–4 sidechain (SC) beads. The features of BB and SC beads have been progressively improved to furnish results comparable to those of all-atom simulations [29]. The secondary structure of proteins may not be conserved in MARTINI-CG based simulations, but this issue can be easily fixed by adding an elastic network to the protein backbone [32]. Of note, very long (hundreds of nanoseconds to microseconds) simulations can be obtained event without the need for high-performance computers and the MARTINI CG force field has been successfully used in combination with WTMDs [33].

In 2013, Limongelli et al. introduced the Funnel Metadynamics (FM), a new tool aimed at further improving the sampling of binding/unbinding events [34]. In FM, a funnel-shaped restraint potential is added to the system to reduce the space to explore in the unbound state. Though in principle FM can be applied to any binding/unbinding system, it has been mainly employed for the study of protein-ligand pairs.

In this work we combined the MARTINI CG approximation with Well-Tempered Funnel Metadynamics (WTFMs) to assess both energy and geometry of the interaction between RBD and hemoglobin (both HbA and HbF). The free energy of interaction was further assessed by means of umbrella sampling (US) simulations [35], while the stability of the proposed interaction geometry was further investigated through unbiased CG-MDs. The biological effects of the RBD/hemoglobin interaction were further confirmed by determining the effect on the mRNA synthesis and release of IL6/8 in IB3–1 cells treated with the isolated S-protein alone and in combination with a 1:1 mixture of HbA:HbF.

2. Material and methods

2.1. Computational methodologies

All the computational methodologies were carried out on a 32 Core AMD Ryzen 93,905×, 3.5 GHz Linux Workstation (O.S. Ubuntu 20.04) equipped with GPU (Nvidia Quadro RTX 4000, 8 GB). All the studies were conducted using Gromacs ver. 2021.1 [36] software patched with plumed ver.2.7.3 [37].

2.2. Preparation of CG structures

The 3D structure for the proteins were derived from the Protein Data Bank (PDB-IDs: 6m0j for RBD and ACE2; 2hhb for $HbA^{T\text{-}state}$; 1bbb for $HbA^{R\text{-}state}$; 1fdh for $HbF^{T\text{-}state}$; 4mqj for $HbF^{R\text{-}state}$; see Table S1 for protein sequences). Water and ions were removed. All-atom structures were converted to the corresponding CG structures through the martinize2 script [38] using the following flags: "-ff martini22"; "-elastic"; "-merge A,B,C,D". The MARTINI heme parameters were derived from the literature [39]. To preserve the interactions between heme co-factors and Hb, harmonic bonds were added between iron atoms and the relevant histidine residues. Each Hb/RBD complex was prepared by randomly placing the hemoglobin close to the accessible surface of RBD. The complexes were then inserted into box of 20x10x10 nm size, aligning the principal axis of the RBD along the x-axis. CG water molecules and ions were then added to solvate and neutralize the complexes. General features of Hb/RBD CG systems are reported in Table S2.

2.3. US simulations of RBD/ACE2 complexe

The CG representation of 6m0j was submitted to energy minimization (steep integrator; number of steps = 10,000; dt = 0.01 ps) and two cycles of equilibration under the NVT conditions at 310 K (md integrator; number of steps = 100,000; dt = 0.01 ps for the first equilibration step and dt = 0.02 ps for the second equilibration step). Standard options for MARTINI simulations were used. During minimization and equilibration, all the BB beads were restrained to their original position. The equilibrated complex was submitted to 50 ns of unbiased MD simulation. The productive phase of the MD was clustered, and the most representative conformation was extracted and submitted to US simulations as follows: the CoG of backbone (BB) atoms of RBD was gradually pulled away from the CoG of BB atoms of ACE2 using a harmonic restraint with a force constant of 150 kJ/mol·nm^2. Then, 20 equally spaced US windows were selected for the complexes with CoG-CoG distances ranging from 4.2 to 8.0 nm. Each US window was run for 35 ns restraining the CoG of RBD in place using a force constant of 300 kJ/mol·nm^2. The Potential of Mean Forces (PMF) was then computed according to the WHAM methodology using the wham.py script (http://membrane.urmc.rochester.edu/?page_id=126). PMFs were thus computed by simulating 700 ns for the complexes. Finally, 100 cycles of Monte-Carlo Bootstrap analysis were run to determine the error associated with the computation of PMFs. The full procedure was repeated applying different scaling factor to the MARTINI22 force field (0.5, 0.6, 0.7, 0.8, 0.9, 1.0). Computed PMF values are reported in Table S3.

2.4. Set up of the funnel restraint potential and WTFMs simulations

The funnel restraint potential was set up according to the original publication. [34] Specific parameters used for each system are reported in Table S4.

All the systems were submitted to energy minimization (steep integrator; number of steps = 10,000; dt = 0.01 ps) and two cycles of equilibration under the NVT conditions at 310 K (md integrator; number of steps = 100,000; dt = 0.01 ps for the first equilibration step and dt = 0.02 ps for the second equilibration step). Standard options for MARTINI simulations were used. During minimization and equilibration, all the BB beads were restrained to their original position. WTMFs simulations were then run under the NVT ensemble with dt = 0.02 ps. The height of the hills added to the CVs was set to 2.092 KJ·mol^{-1} and was progressively reduced applying a biasfactor of 30. Hills were added every 1000 steps. Widths (σ) of the hills were set to 0.1 and 2.0 for CV1 and CV2, respectively. A grid with spacings of 0.02 and 0.4 for CV1 and CV2, respectively, was used to store the hills. Hills, CVs and conformations were strided every 500 steps. Simulations were run until convergence was reached as suggested by the free diffusion along the CVs (Fig. S1) while the heights of the added hills were almost zero and demonstrated by the results of block analysis (Fig. S2). To prevent an excessive drift of the systems, which may have impaired the correct reconstruction of the periodic images and caused crashing errors in the FM approach, a soft restraint potential (20 KJ·mol^{-1}·nm^{-2}) was applied to the CoG of the RBD. WTMFs simulations were reweighted using the plumed driver tool. 1D energy profiles were obtained through the plumed *sum_hills* tool.

2.5. US simulations of RBD/Hb complexes

For each system, the global minimum was extracted and submitted to US simulations as follows: the CoG of backbone (BB) atoms of RBD was gradually pulled away from the CoG of BB atoms of either HbA or HbF using a harmonic restraint with a force constant of 150 kJ/mol·nm^2. Then, 23 equally spaced US windows were selected for the complexes with CoG-CoG distances ranging from 4.2 to 8.5 nm. Each US window was run for 40 ns restraining the CoG of RBD in place using a force constant of 300 kJ/mol·nm^2. The Potential of Mean Forces (PMF) was then computed according to the WHAM methodology using the wham.py script (http://membrane.urmc.rochester.edu/?page_id=126). PMFs were thus computed by simulating 920 ns for the complexes. Finally, 100 cycles of Monte-Carlo Bootstrap analysis were run to determine the error associated with the computation of PMFs.

2.6. Unbiased CG simulations

Global minimum of RBD/$HbA^{T\text{-state}}$ and RBD/$HbF^{R\text{-state}}$, as well as a randomly chosen RBD/$HbA^{T\text{-state}}$ complexes were submitted to 100 ns of unbiased molecular dynamics under the NPT ensemble. Root mean squared deviation (RMSD) values for BB beads were determined through the "gmx rms" tool of Gromacs. In the case of RBD/$HbA^{T\text{-state}}$ and RBD/$HbF^{R\text{-state}}$ the entire MDs were clustered with a cut-off of 0.13 nm.

2.7. Conversion of CG complexes to AA (backmapping)

The most representative cluster for RBD/$HbA^{T\text{-state}}$ and for RBD/$HbF^{R\text{-state}}$ were back-mapped to the AA resolution using the "backward.py" script [40]. In both cases, to improve the quality of the AA model, the initially obtained complex was submitted to 20 ns of unbiased MDs under the Charmm36 force field. The model was evaluated every 5 ns of simulations, measuring the QMEAN, C-beta, all atom and torsion *Z*-scores through the Swiss Model webserver. [41] The conformation obtained at the end of the unbiased MD was then evaluated through the PROCHECK utility available at the PDBsum webserver [42].

2.8. Treatment of IB3–1 cells with S1 spike protein in the presence of HbA and HbF hemoglobins

IB3–1 cells were grown to 60–70 % confluency in LHC8 medium (Thermo Fischer Scientific, Waltham, Massachusetts, USA) supplemented with 5 % fetal bovine serum (FBS, Biowest, Nuaillé, France) in the absence of gentamycin. Cells were exposed to Recombinant SARS-CoV-2 Spike Protein S1 (ab49046, purchased from Abcam, Cambridge, UK), as described elsewhere in the absence or in the presence of a HbA + HbF mixture (Analytical Control Systems Inc., Fishers, IN, USA). The incubation with SARS-CoV-2 Spike protein and HbA/HbF hemoglobins was carried out for 1 h at room temperature. The HbA/HbF solution was used at 1 mM, 3 mM, and 6 mM concentrations, while Recombinant SARS-CoV-2 Spike protein was used at final concentration of 25 nM. The Recombinant SARS-CoV-2 Spike protein in presence or absence of HbA/HbF hemoglobins was added to cells using the procedure described elsewhere [43]. Briefly, after medium removal, cells were incubated for 30 min at 4 °C, with the medium supplemented with LHC8, but in absence of FBS. Then cells were maintained for 30 min at 37 °C, according with the protocol published by Wang et al. After this second incubation, 300 μl of LHC-8 medium supplemented with 5 % (final concentration) of FBS was added to reach the final volume of 500 μl. The cultures were further incubated at 37 °C and for 24 h. After 24 h culturing, the cell supernatant was recovered for Bio-plex analysis and the cells were harvested, lysed and RNA extracted for RT-qPCR analysis.

2.9. RNA isolation

IB-3 cells were harvested using trypsin (0.05 % trypsin and 0.02 % EDTA; Sigma-Aldrich, St. Louis, Missouri, USA), washed with 1 ml of DPBS 1× (Gibco, Thermo Fischer Scientific) and lysed using 1 ml of Tri-Reagent (Sigma Aldrich) for 10^6 cells. Phenol/chloroform extraction procedure was followed to extract RNA. Extracted RNA was washed with cold 75 % ethanol, air-dried, and dissolved in nuclease free pure water. RNA, dissolved in water, was quantified using SmartSpec Plus spectrophotometer (Bio-Rad, Hercules, CA, USA), checked on 1 % agarose gel, to verify its integrity and stored at −80 °C for further analysis.

2.10. RT-qPCR analysis

For gene expression analysis 300 ng of total RNA were reverse transcribed to cDNA, in a final reaction volume of 20 μl, using PrimeScript RT Master Mix (Perfect Real Time) (Takara, Kusatsu, Shiga, Japan). Obtained cDNA was used as template for Real-time-qPCR analysis. RT-qPCR reactions were carried out using gene expression assays, each one composed by a primers pair and a fluorescently labeled 5′ nuclease probe. All employed assays were purchased from IDT (Integrated DNA Technologies, Coralville, Iowa, USA) and sequences of primers and probes are reported in [44]. For each RT-qPCR reaction 2 μl of cDNA were amplified, in presence of 2× PrimeTime Gene Expression Master Mix (Takara) for 40 PCR cycles, using CFX96 Touch Real-Time PCR Detection System (Bio-Rad). Relative expression was calculated using the comparative cycle threshold method (ΔΔCT method). Data were normalized using the human transcripts coding for β-actin, GAPDH and RPL13A as endogenous control. The negative controls: no template cDNA and RT-minus were also run for each assay, to assess the specificity and to rule out contamination. RT-qPCR reactions were performed in duplicate for both target and normalizer sequences. Data were collected and analyzed using Bio-Rad CFX Manager Software Version 1.7 (Bio-Rad) [44,45].

2.11. Bioplex analysis

Cytokines and/or chemokines released by IB-3 cells into their respective supernatants were measured using Bio-Plex Human Cytokine 27-plex Assay (Bio-Rad) following the instruction purchase by the manufacturer and the procedure elsewhere described [45]. The assay allows the multiplexed quantitative measurement of 27 cytokines/chemokines (analyzed proteins include: FGF basic, Eotaxin, G-CSF, GM-CSF, IFN-γ, IL-1β, IL-1ra, IL-2, IL-4, IL-5, IL-6, IL-7, IL-8, IL-9, IL-10, IL-12 (p70), IL-13, IL-15, IL-17 A, IP-10, MCP-1 (MCAF), MIP-1α, MIP-1β, PDGF-BB, RANTES, TNF-α, VEGF) in a single well. 50 μl of cytokine standards or samples (supernatants recovered from IB3–1 cells) were incubated with 50 μl of anti-cytokine conjugated beads in 96-well filter plate for 30 min at room temperature with shaking. The plate was washed by vacuum filtration three times with 100 μl of Bio-Plex Wash Buffer, 25 μl of diluted detection antibody were added to each well and plate was incubated for 30 min at room temperature with shaking. After three filter washes, 50 μl of streptavidin–phycoerythrin were added, and plate was incubated for 10 min at room temperature with shaking. Finally, the plate was washed by vacuum filtration three times, beads were suspended in Bio-Plex Assay Buffer, plate was read by Bio-Rad 96-well plate reader. Data were collected and analyzed by the Bio-Plex Manager Software (Bio-Rad) [45].

3. Results and discussion

3.1. Preparation of CG-structures and set-up of WTFMs

The RBD, $HbA^{T\text{-state}}$, $HbA^{R\text{-state}}$, $HbF^{T\text{-state}}$, and $HbF^{R\text{-state}}$ were converted to the corresponding CG structures using the MARTINI2.2 force field as detailed in the Experimental section. It has been shown that, in some systems, the MARTINI approach tends to overestimate the aggregation of proteins [46]. Accordingly, to verify whether the MARTINI2.2 force field necessitated any correction in the beads interaction potential, we preliminarily computed the CG (un)binding free energy between RBD and ACE2 using scaling factors ranging from 0.5 to 1.0 (original force field) with increments of 0.1 [46] by means of Umbrella Sampling (US) simulations. US belong to the enhancing sampling techniques and has been widely used to compute the free energy difference along a given reaction coordinate [35]. In this work, we used the CoG_{RBD}-CoG_{ACE2} distance as the reaction coordinate. Accordingly, we pulled away the CoG_{RBD}-CoG_{ACE2} from the initial complex (representing the CG representation of the global minimum) to about 8.0 nm. The reaction coordinate was split into 20 windows that were then simulated for 35 ns each (700 ns in total), restraining the CoG_{RBD}-CoG_{ACE2} distance by applying a harmonic potential. The WHAM algorithm was finally used to reconstruct the free energy profile of the (un)binding events. As detailed in Table S3 and Fig. S3, we found that for the system ACE2/RBD the force field did not necessitate any scaling factor to correctly estimate the (un)binding free energy and, thus, we opted for using the unmodified

version of the force field.

Visual inspection of the available structures of the fully glycosylated S-protein [47] confirmed that the RBD can be accessed only in the open state (RBD-up). Conversely, in the closed state (RBD-down), the RBD is completely buried and can not establish interactions with other macromolecules. Additionally, the only part of the RBD that can be accessed even in open state is constituted by the Receptor Binding Motif (RBM; Fig. 2A), that indeed contains all the residues involved in the interactions with the ACE2. The RBM surface is almost isolated in the RBD-up state, and proteins that bind to the RBM are supposed not to interact with other residues of the S-protein. Based on these considerations as well as on the results of SPR experiments, we decided to use only the RBD structure instead of the full S-protein and to include in the funnel restraining potential only the RBM (Fig. 2A,B). The parameters used to define the funnel (length of the cone "z", radius of the cylinder "r", and the amplitude of the cone in radians "α"; Fig. 2B) where chosen to allow an exhaustive sampling of the bound conformation(s) to the RBM as well as the unbound event. Four different WTFMs simulations (RBD/HbA$^{T\text{-state}}$; RBD/HbA$^{R\text{-state}}$; RBD/HbF$^{T\text{-state}}$; RBD/HbF$^{R\text{-state}}$) were run until the convergence was reached (6 μs for RBD/HbA$^{T\text{-state}}$; 5 μs for all the other protein pairs. Fig. S4). The distance between the center of geometry (CoG) of RBD and the CoG of HbA (or HbF) was used as the first CV (i.e., CV1 = CoG_{RBD}-CoG_{Hb} distance), aiming at distinguishing between the bound and the unbound state. To account for the different binding geometries and considering the ellipsoidal symmetry of Hb, we computed a second CV based on "pseudocontacts" (PCs). In detail, a residue of the HbA(HbF) established a PC if its BB bead falls within 2 nm from any of the BB bead of the RBM residues. Then, CV2 (ΔPCs) was computed as follow:

$$\Delta PCs_{(A)} = (PCs_{RBD-\alpha n} + PCs_{RBD-\alpha m}) - (PCs_{RBD-\beta n} + PCs_{RBD-\beta m}) \text{ for RBD/HbA}$$

$$\Delta PCs_{(F)} = (PCs_{RBD-\gamma n} + PCs_{RBD-\gamma m}) - (PCs_{RBD-\beta n} + PCs_{RBD-\beta m}) \text{ for RBD/HbF}$$

Fig. 2B and C shows the BB of RBD and HbA, respectively, considered to compute the PCs. Clarifying examples of CV2 computation are also reported in Fig. S5, whereas the RBM residues are highlighted in Table S1.

3.2. Analysis of WTFMs and (un)binding free energy determination

The results from the four WTFMs were reweighted according to the scheme proposed by Branduardi et al. [48] to reconstruct the FES as function of CV1 and CV2 (Fig. 3A-D, left).

Of note, the original states (either R or T) of both HbA and HbF were preserved during the simulations thanks to the application of the ELNEDYN [32] elastic network approach (see experimental section for more details), thus overcoming the known issue of T- > R state transition in hemoglobin MDs [49]. According to the FM protocol we also calculated the $\Delta G_{(un)binding}$ by considering the difference in the free energy between the global minimum (yellow stars in Fig. 3) and the average energy value assumed in the unbound state (characterized by CoG distance values between 7.0 and 7.5 nm).

The ΔG values (corrected considering the entropic effect of the funnel potential; [34] Table 1) suggested that the binding order preference was: HbA$^{T\text{-state}}$ ≈ HbF$^{R\text{-state}}$ > HbA$^{R\text{-state}}$ > HbF$^{T\text{-state}}$. Thus, in the case of HbA, the interaction of the unliganded form was preferred. This observation is in line with the experiments of Dyankov et al. [24] who showed that blowing carbon monoxide in incubated biochips did not lead to changes in the SPR signal. While the authors proposed a direct interaction with the heme co-factor, our data suggest that the inability to adsorb CO might be related to the more favorable T-state assumed by the HbA in the complex with the RBD than the R-state.

Indeed, visual inspection of the global minimum conformations (see Fig. 3A-D, right) suggested that heme co-factors were not involved in the binding. The preferred geometry of interaction was RBD/$\alpha_n\beta_n$ for HbA and RBD/$\alpha_n\gamma_n$ for HbF, independently from the R- or T-states. This means that the minor plane of the hemoglobin ellipsoid tended to lay parallel to the interacting plane of the RBD (see also Fig. 1 for a schematic representation of hemoglobin). Conversely, RBD/$\alpha_n\beta_m$ and RBD/$\alpha_n\gamma_m$ interacting geometries (in which the minor plane of the ellipsoid would have lie perpendicular to the plane of the RBD) were only poorly visited. Indeed, RBD/$\alpha_n\beta_m$ RBD/and $\alpha_n\gamma_m$ complexes were expected to be characterized by CoG distances lower than 4.5 nm due to the ellipticity of the hemoglobin but, as it can be seen in Fig. 3, at these values only relatively high energy conformations were found.

To verify that the simulations exhaustively sampled all the rotatory orientations of the HbA(F), we measured the x-, y-, and z-components of the radius of gyration of the hemoglobin as a function of CoG-CoG distance (see Fig. S6–9). Of note, both the initial CoG-CoG distance as well as the initial HbA(F) relative orientation to the RBF were not correlated with those of the global minima, suggesting that the randomly chosen starting state did not influence the final complexes. To further demonstrate this aspect, we then conducted a second replica simulation for the RBD/HbF$^{R\text{-state}}$ system starting from a completely different initial conformation. Indeed, the results obtained in terms of both the FES (Fig. S10) and of the x-, y-, and z-components of the radius of gyration (Fig. S11) largely agreed with those of the first replica.

The added bias potential was also reweighted using two different variables, i.e. the number of PCs between RBD and $\alpha_n + \alpha_m$ (or $\gamma_n + \gamma_m$)

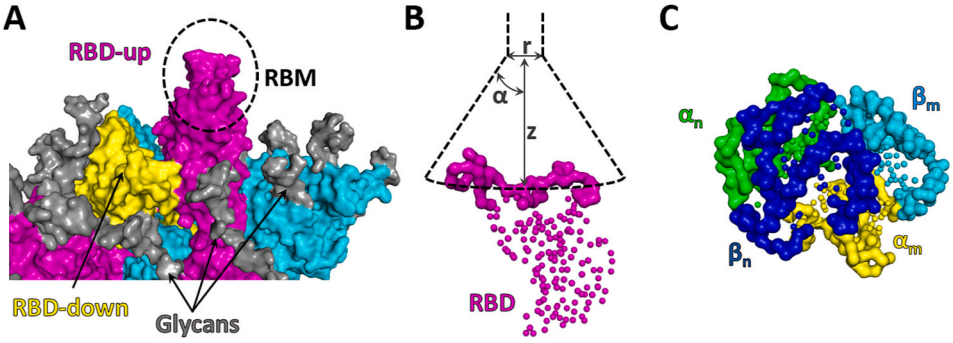

Fig. 2. Representation of structures used. A) Surface representation of full trimeric S-protein with one RBD-up domain (magenta). The Receptor Binding Motif of the RBD (RBM, i.e., the surface that recognizes the ACE2) is highlighted. Glycans are shown as gray surfaces. B) CG representation of backbone beads of RBD and features of the funnel used in WTFMs. Beads belonging to the RBM are represented as surface, whereas beads not involved in binding are represented as spheres. The geometrical features of the funnel (r, z, α) are also indicated. Note that only the CoG of the "ligand" (i.e., the hemoglobin in this work) is forced inside the funnel during the simulations. C) CG representation of backbone beads of Hb. Beads belonging to the external surface are represented as surface, whereas beads not involved in binding are represented as spheres. (For interpretation of the references to colour in this figure legend, the reader is referred to the web version of this article.)

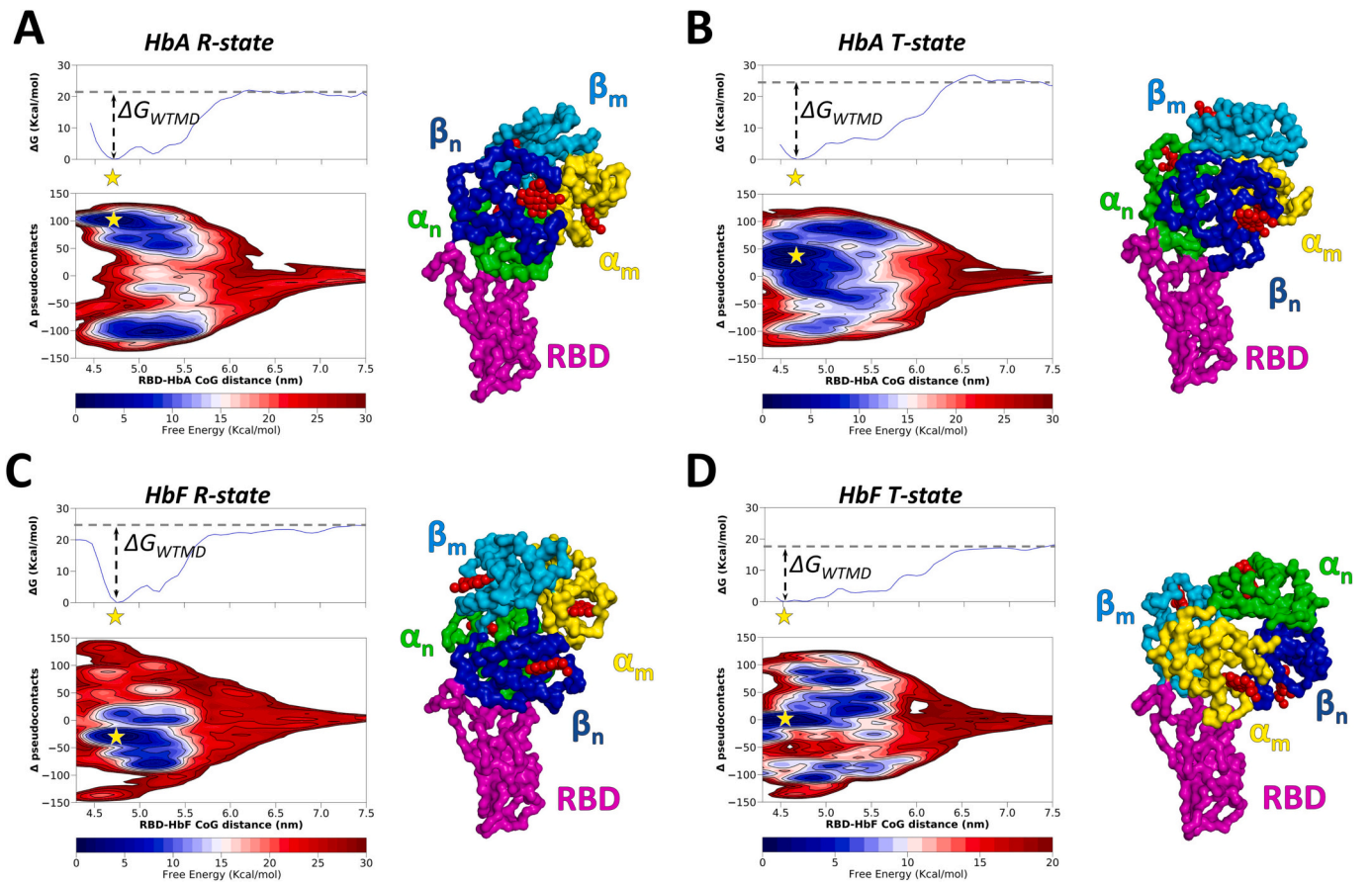

Fig. 3. Results of the WTMFs simulations. All panels show the 1D energy profile (top left), the FES for the RBD/Hb interaction (bottom left) and the extracted structure of the global minimum (right; only BB beads have been used to represent the complexes. Heme residues are also shown as red spheres). The yellow star in each FES indicates the global minimum. A) RBD/HbA$^{R\text{-state}}$. B) RBD/HbA$^{T\text{-state}}$. C) RBD/HbF$^{R\text{-state}}$. D) RBD/HbF$^{T\text{-state}}$. (For interpretation of the references to colour in this figure legend, the reader is referred to the web version of this article.)

Table 1
$\Delta G_{(un)binding}$ values obtained through biased molecular dynamics.

	ΔG WTFM (Kcal/mol)	ΔG US (Kcal/mol)	Average ΔG (Kcal/mol)
RBD/HbA$^{R\text{-state}}$	−21.26 ± 0.39	−21.11 ± 0.15	−21.19 ± 0.42
RBD/HbA$^{T\text{-state}}$	−23.37 ± 0.39	−21.95 ± 0.16	−22.66 ± 0.42
RBD/HbF$^{R\text{-state}}$	−24.64 ± 0.41	−23.58 ± 0.14	−24.11 ± 0.43
RBD/HbF$^{T\text{-state}}$	−18.23 ± 0.41	−18.60 ± 0.15	−18.42 ± 0.44

chains and between RBD and $\beta_n + \beta_m$ chains (Fig. S12). For all the systems, the global minima were characterized by a total number of about 140 PCs, indicating a good complementarity between the proteins, consistent with the highly favorable $\Delta G_{binding}$ values. HbA$^{R\text{-state}}$ interacted with RBD mainly through one α chain, whereas in all the other cases the interaction involved both one α and one β (or γ) chains in a more balanced way.

To verify whether the use of the funnel restraint potential may have affected the computation of the $\Delta G_{(un)binding}$, we submitted the global minima conformations to US simulations using the CoG_{RBD}-CoG_{Hb} distance as the reaction coordinates. According to the RBD/ACE2 simulations described above, we pulled away the CoG_{RBD}-CoG_{Hb} from the global minima to about 8.0 nm thus sampling in a more exhaustive way the unbound regions than in the WTFMs. The reaction coordinate was split into 20 windows (Fig. S13) that were then simulated for 35 ns each (700 ns in total), restraining the CoG_{RBD}-CoG_{Hb} distance by applying a harmonic potential. The WHAM algorithm was finally used to reconstruct the free energy profile of the (un)binding events (Fig. 4). The convergence of US simulations was assessed by comparing the ΔG profiles at different simulation times (Fig. S14). As reported in Table 1, the ΔG_{US} values were in good agreement with ΔG_{WTFM} values, confirming the feasibility to apply the FM approach to protein-protein interactions.

3.3. Binding mode analysis

According to the ΔG values from both WTFMs and US simulations, the global minima of RBD/HbA$^{T\text{-state}}$ and RBD/HbF$^{R\text{-state}}$ were chosen as the most probable interaction geometries between the S-protein and the adult or fetal hemoglobin, respectively.

The two complexes were submitted to 100 ns of unbiased CG-MDs (Fig. 5A,B). In parallel, to verify that the unbiased MDs were long enough to eventually catch any complex instability, one RBD/HbA$^{T\text{-state}}$ structure not corresponding to the global minimum was randomly chosen and submitted to 100 ns of unbiased MDs (Fig. 5C). RMSD values (measured on BB beads) confirmed that the chosen global minima were very stable, whereas the non-minimum structure readily underwent marked structural changes.

Unbiased MDs for RBD/HbA$^{T\text{-state}}$ and RBD/HbF$^{R\text{-state}}$ were clustered and, for both, the most representative conformation was extracted and reconverted to the AA representation as previously reported. [40] Final

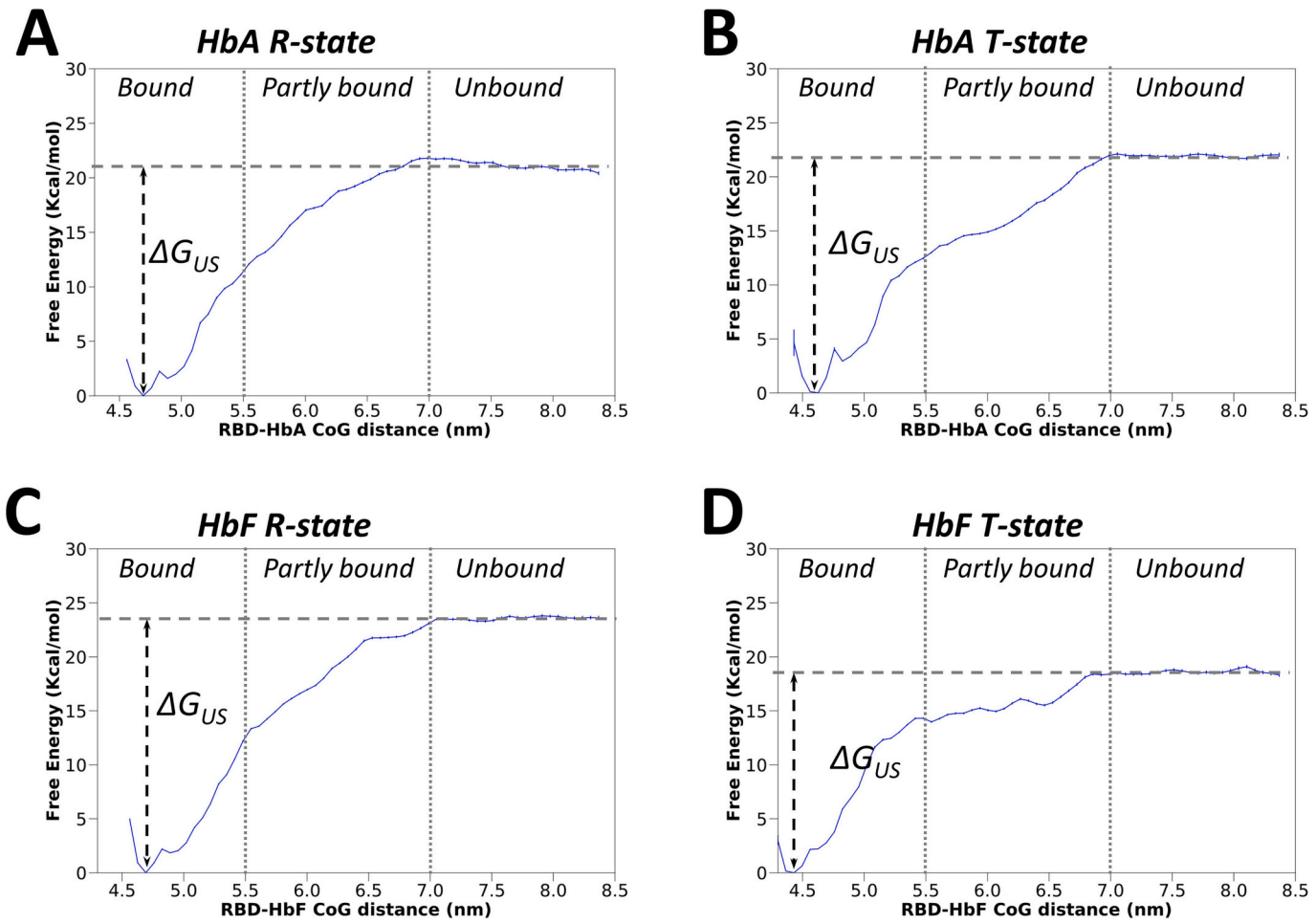

Fig. 4. 1D energy profile obtained from US simulations. A) RBD/HbA$^{R\text{-state}}$. B) RBD/HbA$^{T\text{-state}}$. C) RBD/HbF$^{R\text{-state}}$. D) RBD/HbF$^{T\text{-state}}$.

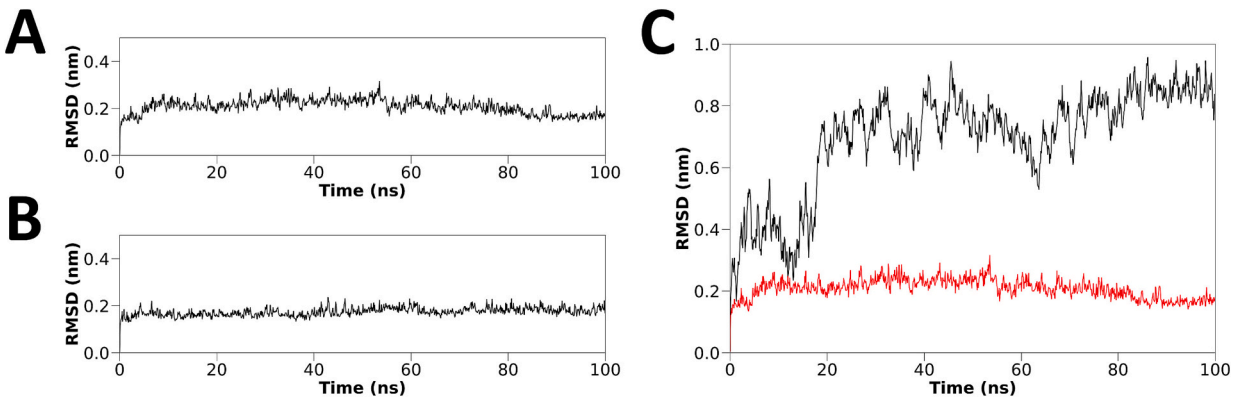

Fig. 5. Results of unbiased CG-MDs. A) RMSD (backbone beads; nm) for RBD/HbA$^{T\text{-state}}$ global minimum. B) RMSD (backbone beads; nm) for RBD/HbF$^{R\text{-state}}$ global minimum. C) Comparison of RMSD values obtained for one randomly selected non-global minimum RBD/HbA$^{T\text{-state}}$ conformation (black line) and for RBD/HbA$^{T\text{-state}}$ global minimum (red line. The RMSD values are the same as in panel A). (For interpretation of the references to colour in this figure legend, the reader is referred to the web version of this article.)

models quality was assessed through the SwissModel and PDBsum webservers. By submitting the initially back-mapped (i.e., CG to AA) structures to short (20 ns) unbiased MD simulations, the final structures reached overall medium to good qualities, as shown by the overall QMEAN scores (−2.12 and − 2.30 for RBD/HbA$^{T\text{-state}}$ and RBD/HbF$^{R\text{-state}}$ respectively; Fig. S15). Ramachandran plots (Fig. S16), Phi-Psi, Chi1-Chi2, Chi3 and Chi4 distributions (Figs. S17–18) further confirmed the goodness of the computed models. However, torsion *Z*-score (from SwissModel) and Omega dihedral angles distribution (from PDBsum) agreed in suggesting that the models could be further improved.

The PDBsum webserver was also used to derive the intermolecular interactions (Fig. 6 and Figs. S19-S20). In accordance with the favorable binding energy determined through WTMF and US simulations, the RBD and HbA(F) interacted through extensive networks of bonded (hydrogen bonds and salt bridges) and non-bonded (lipophilic) interactions which

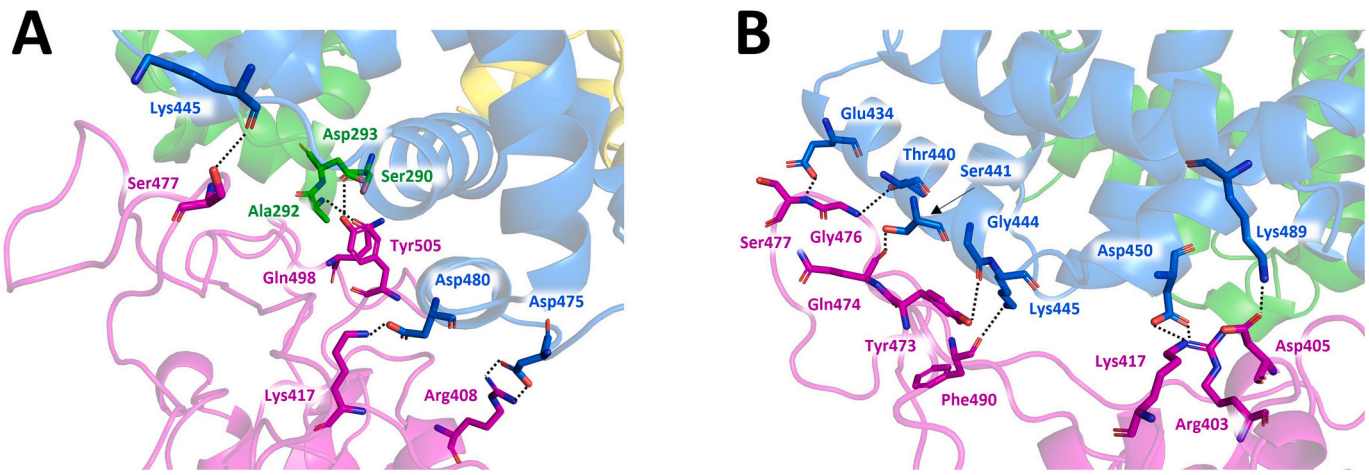

Fig. 6. Details of the interactions between Hb and the RBM of the RBD. Residues involved in intermolecular interactions are highlighted as sticks. RBD is colored in pink; Hb backbone is colored in dark green (for α chains) or blue (for β and γ chains). Hydrogen bonds and salt bridges are highlighted as black dashed lines. A) RBD/$HbA^{T\text{-state}}$ complex. B) RBD/$HbF^{R\text{-state}}$ complex. (For interpretation of the references to colour in this figure legend, the reader is referred to the web version of this article.)

involved the entire RBM.

As expected, when the obtained complexes were superimposed to the fully glycosylated Spike protein model [47], The Hb molecules did not show any interactions with other parts of the virus protein (Fig. S21).

3.4. Human hemoglobins interfere with SARS-CoV-2 mediated biological effects on human bronchial epithelial IB3–1 cells

To obtain biological data supporting the bioinformatic analysis, we have employed an experimental model system based on the human bronchial epithelial IB3–1 cell line. This system has been described by Gasparello et al. [44,45] and is represented in Fig. 7A. When IB3–1 cells are exposed to SARS-CoV-2 Spike protein, reproducible effects are obtained, including activation of NF-κB, and increase in the expression of NF-κB dependent genes, such as those encoding interleukin-6 (IL-6) and IL-8. These changes in gene expression can be easily investigated by using RT-qPCR based biomolecular analysis. We have reported that, fully in agreement with the SARS-CoV-2 mediated changes in gene expression, the extracellular release of IL-6 and IL-8 increases. This can be easily demonstrated by performing a Bioplex analysis of the supernatant of IB3–1 treated cells. Using this validated model system, we investigated the effects of human hemoglobins on the SARS-CoV-2 mediated effects, as reported in the scheme depicted in Fig. 7A. We employed a hemoglobin mixture composed by about 50 % HbA and about 50 % HbF, as demonstrated by the HPLC analysis shown in Fig. 6B. As expected, the administration of the virus protein alone caused a marked increase in the expression of IL-6 (Fig. 7C) and IL-8 (Fig. 7D) mRNA as well as in the release of the cytokines (Fig. 7E). The pre-treatment of SARS-CoV-2 S-protein with 1, 3 and 6 μM of the hemoglobins mixture (Fig. 7C-E) led to a sharp decrease of accumulation of IL-6 and IL-8 mRNA, after comparison with control IB3–1 cells exposed to SARS-CoV-2 in the absence of pre-treatment with the Hb mixture. The inhibitory effects of the Hb mixture were observed even with the lower dose used (1 μM) when both IL-6 (Fig. 7C) and IL-8 (Fig. 7D) mRNAs were assayed by RT-qPCR. The same conclusion was reached when β-actin, GAPDH and RPL13 housekeeping RNA sequences were used as internal controls (Fig. S10, panels A-D). Fully in agreement, the extracellular release of IL-6 and IL-8 was found reduced in IB3–1 cells exposed to SARS-CoV-2 S protein pre-treated with 1 μM of the Hb mixture. This is demonstrated by the Bioplex analysis shown in Fig. 7E. In agreement, also the expression of other pro-inflammatory genes (IL-5, G-CSF, GM-CSF) was found reduced in IB3–1 cells exposed to SARS-CoV-2 S protein pre-treated with 1 μM of the Hb mixture (Fig. S22, panels D and F). Altogether, these results support the finding that RDB can bind HbF and HbA with high efficiency.

The data obtained on the inhibitory effects of the Hb mixture on Spike effects on IB3–1 cells are of interest also in respect to previously reported studies on the protective effects of isolated HbA against SARS-CoV-2 infection [23]. In addition, it has also been reported that the S-protein induces pro-inflammatory effects in human cells [44,50]. We confirm that IL-6 and IL-8 genes are upregulated in S-protein exposed IB3–1 cells and that human hemoglobins interferes with S-protein activity (Fig. 7, C-E) possibly through molecular interactions, as highlighted by our MDs experiments. We like to underline that the 1:1 HbA + HbF mixture employed (Fig. 7B) is relevant for the issue regarding the effects of S-protein in β-thalassemia, since it mimics the hemoglobin pattern of β^{+}/β^{0} thalassemia patients (for instance the patients carrying the β^{+}-IVS-110/β^{0}39 genotype). Our data suggest that exposure to S-protein might impair the hemoglobin-mediated functions in erythroid cells from those patients. In future studies, the experiment depicted in Fig. 7 should be performed using purified HbA or purified HbF, in order to obtain information on the possible impact of S-protein/HbA or S-protein/HbF interactions on biological functions of erythroid cells from healthy adults (producing HbA and lacking, or expressing at very low levels, HbF) or from homozygous β^{0}/β^{0} thalassemia patients (for instance those carrying a $\beta^{0}39/\beta^{0}39$ phenotype, producing HbF, but lacking HbA).

4. Conclusions

In this paper we have investigated the geometry and the energy of the interaction between the RBD and both the human adult (HbA) and fetal (HbF) hemoglobin by means of enhanced sampling molecular dynamics techniques. By applying the MARTINI-CG approximation, we were able to conduct long simulations without the need for specialized high-performance computing. Indeed, each system was simulated for more than 5 μs in less than 2 days by using an easy affordable workstation (see Experimental Section for technical details). Besides, by applying the elastic network approach implemented in the MARTINI-CG dynamics, we overcome the known issue of T- > R transition in hemoglobin MDs and were thus able to distinguish between the ability of T-states and R-states to bind the S-protein. The simulations suggested that the most probable conformations interacting with the RBD were the T-state for HbA and R-state for HbF. Our data agree with previously reported biochemical results [23,24], while providing a different rational hypothesis as to why RBD/HbA is unable to adsorb carbon monoxide.

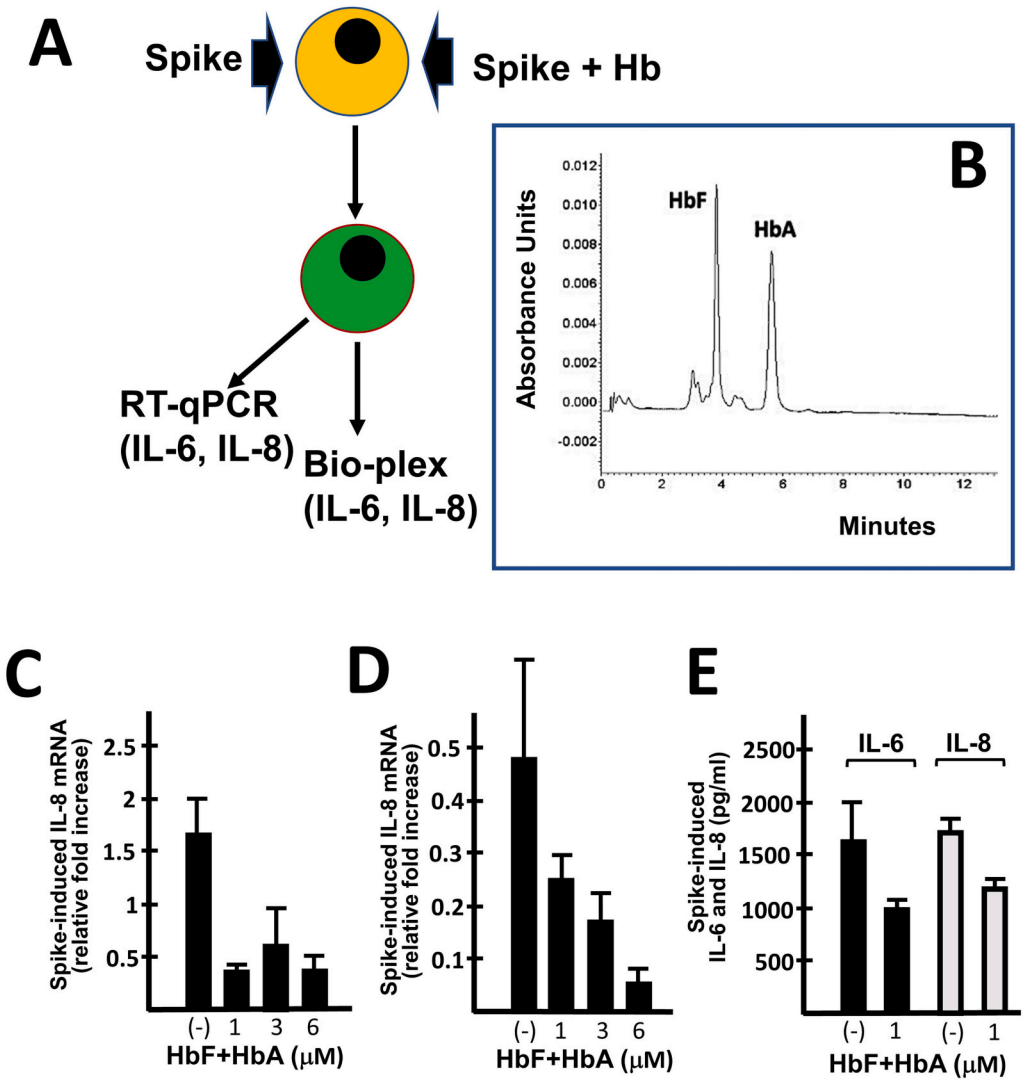

Fig. 7. Impacts of hemoglobins on proinflammatory effects exerted by SARS-CoV-2 S-protein in IB3–1 cells. A) IB3–1 cells have been exposed to SARS-CoV-2 S-protein in the absence or in the presence of a 1:1 HbA:HbF mixture. After a washing step and 48 h culturing, the cells have been harvested, RNA extracted, and RT-qPCR performed using primers amplifying IL-6 and IL-8 mRNA sequences. Supernatants were also isolated for the analysis of secreted proteins by the Bio-plex methodology. B) HPLC analysis of the HbA:HbF mixture. C,D) Effects of the pre-treatment of the SARS-CoV-2 S-protein with 1, 3 and 6 μM of the hemoglobin mixture. Results represent the fold increase of mRNA Content with respect to untreated IB3–1 cells, cultured in parallel for the same time (48 h). E) Reduction of secreted IL-6 and IL-8 when IB3–1 cells have been cultured for 48 h following exposure to SARS-CoV-2 Spike protein in the absence (−) or in the presence of 1 μM hemoglobin mixture.

In all the cases, the hemoglobin interacted with the RBD through the $\alpha_n\beta(\gamma)_n$ surface and both RBD/HbA$^{T\text{-state}}$ and RBD/HbF$^{R\text{-state}}$ showed very favorable interactions ($\Delta G < -20$ Kcal/mol). Indeed, when epithelial cells were co-cultured with 1:1 mixture of HbA:HbF and S-protein, a marked reduction in the pro-inflammatory effect exerted by the virus protein was observed.

Overall, our data further confirm the hypothesis of a direct binding between hemoglobin and S-protein and provide a plausible model of their binding geometry. The binding energy determined in this paper is substantially more favorable than those obtained solely by docking engine [Gambari, submitted paper], suggesting that the more thorough exploration of the chemical space obtained through molecular dynamics can led to more reliable and exhaustive results. Besides, to the best of our knowledge, this work represents the first example of the application of the funnel metadynamics strategy for the study of protein-protein interaction. Conversion of the CG complexes to the AA representation by means of the backmapping strategy developed for the MARTINI forcefield along with short unbiased MD simulations led to overall medium to good models, with the limiting factor in the quality being the distribution of torsion angles. We believe that our approach can be successfully applied in the future to derive structural data for other large systems and to derive at least preliminary hypotheses on the geometry of the unknown protein-protein interaction. Limitations of our approach regard the following aspects. First, the use of an elastic network (necessary in the context of MARTINI-based simulations to preserve the protein secondary structure) that limits the full conformational space exploration for very flexible protein. An alternative to the elastic network could be in principle the use of the GO-MARTINI approach [51] which is based on the use of additional Lennard-Jones potentials between close interacting particles. It must be pointed out, however, that GO-MARTINI models can be less stable than elastic network-based ones due to sudden increase of the potential energy related to the repulsive component of the additional Lennard-Jones potentials. Second, the CG representation of proteins obviously causes the loss of some information because of the simplification introduced with the force field. This is reflected by the non-optimal quality of the final model. Third, the

MARTINI force field may require some tuning, based on an available and suitable model system (e.g., the complex RBD/ACE2 in the present work) to produce a reliable PMF profile.

Our study suggests that the effects of the S protein on the hematopoietic system should be studied in deep, using in vitro and ex vivo erythroid cellular systems or, in real world, studying not only COVID-19 patients, but also in people undergoing COVID-19 vaccination. In fact, production of S-protein occurs not only following SARS-CoV-2 infection, but also after the administration of the mRNA-based RNA vaccines, such as Comirnaty (BNT162b2) and Spikevax (mRNA-1273) COVID-19 vaccines [52].

CRediT authorship contribution statement

JG, MV, AC, RG, and GM curated data and performed experiments. RG and GM acquired funding. RG and GM designed and supervised the study. RG and GM wrote the original draft. JG, MV, AC, RG, and GM wrote, reviewed and edited the manuscript. All authors have read and approved the final version of the manuscript.

Declaration of competing interest

The authors declare that they have no known competing financial interests or personal relationships that could have appeared to influence the work reported in this paper.

Acknowledgements

The present study was supported by the CARIPARO Foundation (grant no. MARZ_CARIVARI20_01 C94I20002500007), the MUR-FISR COVID-miRNAPNA Project (grant no. FISR2020IP_04128), the Inter-university Consortium for Biotechnologies in Italy (grant no. CIB-Unife-2020-1), and the FIRC-AIRC 'Michele e Carlo Ardizzone' fellowship (grant no. 25528).

Appendix A. Supplementary data

Supplementary data to this article can be found online at https://doi.org/10.1016/j.ijbiomac.2023.127088.

References

[1] B. Hu, H. Guo, P. Zhou, Z.L. Shi, Characteristics of SARS-CoV-2 and COVID-19, Nat. Rev. Microbiol. 19 (3) (2021) 141–154.
[2] C. Chakraborty, A.R. Sharma, M. Bhattacharya, G. Agoramoorthy, S.S. Lee, The drug repurposing for COVID-19 clinical trials provide very effective therapeutic combinations: lessons learned from major clinical studies, Front. Pharmacol. 12 (2021) 704205.
[3] M. Li, H. Wang, L. Tian, Z. Pang, Q. Yang, T. Huang, J. Fan, L. Song, Y. Tong, H. Fan, COVID-19 vaccine development: milestones, lessons and prospects, Signal Transduct. Target. Ther. 7 (1) (2022) 146.
[4] H.E. Davis, L. McCorkell, J.M. Vogel, E.J. Topol, Long COVID: major findings, mechanisms and recommendations, Nat. Rev. Microbiol. 21 (3) (2023) 133–146.
[5] W. Yan, Y. Zheng, X. Zeng, B. He, W. Cheng, Structural biology of SARS-CoV-2: open the door for novel therapies, Signal Transduct. Target. Ther. 7 (1) (2022) 26.
[6] J. Shang, G. Ye, K. Shi, Y. Wan, C. Luo, H. Aihara, Q. Geng, A. Auerbach, F. Li, Structural basis of receptor recognition by SARS-CoV-2, Nature 581 (7807) (2020) 221–224.
[7] Q. Wang, S.B. Ye, Z.J. Zhou, A.L. Song, X. Zhu, J.M. Peng, R.M. Liang, C.H. Yang, X. W. Yu, X. Huang, J. Yu, Y. Qiu, X.Y. Ge, Key mutations in the spike protein of SARS-CoV-2 affecting neutralization resistance and viral internalization, J. Med. Virol. 95 (1) (2023), e28407.
[8] N. Eslami, P.S. Aghbash, A. Shamekh, T. Entezari-Maleki, J.S. Nahand, A.J. Sales, H.B. Baghi, SARS-CoV-2: receptor and co-receptor tropism probability, Curr. Microbiol. 79 (5) (2022) 133.
[9] J. Liu, Y. Li, Q. Liu, Q. Yao, X. Wang, H. Zhang, R. Chen, L. Ren, J. Min, F. Deng, B. Yan, L. Liu, Z. Hu, M. Wang, Y. Zhou, SARS-CoV-2 cell tropism and multiorgan infection, Cell Discov 7 (1) (2021) 17.
[10] Y. Guo, V. Kanamarlapudi, Molecular analysis of SARS-CoV-2 spike protein-induced endothelial cell permeability and vWF secretion, Int. J. Mol. Sci. 24 (6) (2023).
[11] M. Kucia, J. Ratajczak, K. Bujko, M. Adamiak, A. Ciechanowicz, V. Chumak, K. Brzezniakiewicz-Janus, M.Z. Ratajczak, An evidence that SARS-Cov-2/COVID-19 spike protein (SP) damages hematopoietic stem/progenitor cells in the mechanism of pyroptosis in Nlrp3 inflammasome-dependent manner, Leukemia 35 (10) (2021) 3026–3029.
[12] R. Kronstein-Wiedemann, M. Stadtmüller, S. Traikov, M. Georgi, M. Teichert, H. Yosef, J. Wallenborn, A. Karl, K. Schütze, M. Wagner, A. El-Armouche, T. Tonn, SARS-CoV-2 infects red blood cell progenitors and dysregulates hemoglobin and Iron metabolism, Stem Cell Rev. Rep. 18 (5) (2022) 1809–1821.
[13] M. Jha, M.L. Tak, R. Gupta, P. Sharma, V. Rajpurohit, P. Mathur, N. Gaur, Relationship of anemia with COVID-19 deaths: a retrospective cross-sectional study, J. Anaesthesiol. Clin. Pharmacol. 38 (Suppl. 1) (2022) S115–S119.
[14] M. Anai, K. Akaike, H. Iwagoe, T. Akasaka, T. Higuchi, A. Miyazaki, D. Naito, Y. Tajima, H. Takahashi, T. Komatsu, A. Masunaga, H. Kishi, K. Fujii, K. Fukuda, Y. Tomita, S. Saeki, H. Ichiyasu, T. Sakagami, Decrease in hemoglobin level predicts increased risk for severe respiratory failure in COVID-19 patients with pneumonia, Respir. Investig. 59 (2) (2021) 187–193.
[15] G. Lippi, C. Mattiuzzi, Hemoglobin value may be decreased in patients with severe coronavirus disease 2019, Hematol Transfus Cell Ther 42 (2) (2020) 116–117.
[16] M.F. Perutz, Mechanisms regulating the reactions of human hemoglobin with oxygen and carbon monoxide, Annu. Rev. Physiol. 52 (1990) 1–25.
[17] M.R. Mihailescu, I.M. Russu, A signature of the T —> R transition in human hemoglobin, Proc. Natl. Acad. Sci. U. S. A. 98 (7) (2001) 3773–3777.
[18] A. Wilber, A.W. Nienhuis, D.A. Persons, Transcriptional regulation of fetal to adult hemoglobin switching: new therapeutic opportunities, Blood 117 (15) (2011) 3945–3953.
[19] E.F. McCarthy, The oxygen affinity of human maternal and foetal haemoglobin, J. Physiol. 102 (1) (1943) 55–61.
[20] A.T. Taher, K.M. Musallam, M.D. Cappellini, β-Thalassemias, N Engl J Med 384 (8) (2021) 727–743.
[21] E. Gallo, P. Massaro, R. Miniero, D. David, C. Tarella, The importance of the genetic picture and globin synthesis in determining the clinical and haematological features of thalassaemia intermedia, Br. J. Haematol. 41 (2) (1979) 211–221.
[22] R. Gambari, E. Fibach, Medicinal chemistry of fetal hemoglobin inducers for treatment of beta-thalassemia, Curr. Med. Chem. 14 (2) (2007) 199–212.
[23] G.C. Lechuga, F. Souza-Silva, C.Q. Sacramento, M.R.O. Trugilho, R.H. Valente, P. Napoleão-Pêgo, S.S.G. Dias, N. Fintelman-Rodrigues, J.R. Temerozo, N. Carels, C.R. Alves, M.C.S. Pereira, D.W. Provance, T.M.L. Souza, S.G. De-Simone, SARS-CoV-2 proteins bind to hemoglobin and its metabolites, Int. J. Mol. Sci. 22 (16) (2021).
[24] G. Dyankov, P. Genova-Kalou, T. Eftimov, S.S. Ghaffari, V. Mankov, H. Kisov, P. Veselinov, E. Hikova, N. Malinowski, Binding of SARS-CoV-2 structural proteins to hemoglobin and myoglobin studied by SPR and DR LPG, Sensors (Basel) 23 (6) (2023).
[25] X. Wu, L.Y. Xu, E.M. Li, G. Dong, Application of molecular dynamics simulation in biomedicine, Chem. Biol. Drug Des. 99 (5) (2022) 789–800.
[26] R.C. Bernardi, M.C.R. Melo, K. Schulten, Enhanced sampling techniques in molecular dynamics simulations of biological systems, Biochim. Biophys. Acta 1850 (5) (2015) 872–877.
[27] A. Barducci, G. Bussi, M. Parrinello, Well-tempered metadynamics: a smoothly converging and tunable free-energy method, Phys. Rev. Lett. 100 (2) (2008), 020603.
[28] T.M. Schäfer, G. Settanni, Data reweighting in Metadynamics simulations, J Chem Theory Comput 16 (4) (2020) 2042–2052.
[29] S.J. Marrink, H.J. Risselada, S. Yefimov, D.P. Tieleman, A.H. de Vries, The MARTINI force field: coarse grained model for biomolecular simulations, J. Phys. Chem. B 111 (27) (2007) 7812–7824.
[30] B.M.H. Bruininks, P.C.T. Souza, S.J. Marrink, A practical view of the Martini force field, Methods Mol. Biol. 2022 (2019) 105–127.
[31] S.J. Marrink, L. Monticelli, M.N. Melo, R. Alessandri, D.P. Tieleman, P.C.T. Souza, Two decades of Martini: better beads, broader scope, WIREs Computational Molecular Science 13 (1) (2023), e1620.
[32] X. Periole, M. Cavalli, S.J. Marrink, M.A. Ceruso, Combining an elastic network with a coarse-grained molecular force field: structure, dynamics, and intermolecular recognition, J Chem Theory Comput 5 (9) (2009) 2531–2543.
[33] C. Lamprakis, I. Andreadelis, J. Manchester, C. Velez-Vega, J.S. Duca, Z. Cournia, Evaluating the efficiency of the Martini force field to study protein dimerization in aqueous and membrane environments, J Chem Theory Comput 17 (5) (2021) 3088–3102.
[34] V. Limongelli, M. Bonomi, M. Parrinello, Funnel metadynamics as accurate binding free-energy method, Proc. Natl. Acad. Sci. U. S. A. 110 (16) (2013) 6358–6363.
[35] J. Kästner, Umbrella sampling, WIREs Comput. Mol. Sci. 1 (6) (2011) 932–942.
[36] D. Van Der Spoel, E. Lindahl, B. Hess, G. Groenhof, A.E. Mark, H.J. Berendsen, GROMACS: fast, flexible, and free, J. Comput. Chem. 26 (16) (2005) 1701–1718.
[37] P. Consortium, Promoting transparency and reproducibility in enhanced molecular simulations, Nat Methods 16 (8) (2019) 670–673.
[38] P.C. Kroon, F. Grünewald, J. Barnoud, M. van Tilburg, P.C. Souza, T.A. Wassenaar, S.-J. Marrink, Martinize2 and vermouth: unified framework for topology generation, eLife 12 (2023). RP90627.
[39] D.H. de Jong, N. Liguori, T. van den Berg, C. Arnarez, X. Periole, S.J. Marrink, Atomistic and coarse grain topologies for the cofactors associated with the photosystem II Core complex, J. Phys. Chem. B 119 (25) (2015) 7791–7803.
[40] T.A. Wassenaar, K. Pluhackova, R.A. Böckmann, S.J. Marrink, D.P. Tieleman, Going backward: a flexible geometric approach to reverse transformation from coarse grained to atomistic models, J. Chem. Theory Comput. 10 (2) (2014) 676–690.
[41] P. Benkert, M. Biasini, T. Schwede, Toward the estimation of the absolute quality of individual protein structure models, Bioinformatics 27 (3) (2011) 343–350.

[42] R.A. Laskowski, M.W. MacArthur, D.S. Moss, J.M. Thornton, PROCHECK: a program to check the stereochemical quality of protein structures, J. Appl. Cryst. 26 (2) (1993) 283–291.
[43] W. Wang, L. Ye, B. Li, B. Gao, Y. Zeng, L. Kong, X. Fang, H. Zheng, Z. Wu, Y. She, Up-regulation of IL-6 and TNF-alpha induced by SARS-coronavirus spike protein in murine macrophages via NF-kappaB pathway, Virus Res. 128 (1–2) (2007) 1–8.
[44] J. Gasparello, E. D'Aversa, C. Papi, L. Gambari, B. Grigolo, M. Borgatti, A. Finotti, R. Gambari, Sulforaphane inhibits the expression of interleukin-6 and interleukin-8 induced in bronchial epithelial IB3-1 cells by exposure to the SARS-CoV-2 spike protein, Phytomedicine 87 (2021) 153583.
[45] J. Gasparello, E. d'Aversa, G. Breveglieri, M. Borgatti, A. Finotti, R. Gambari, In vitro induction of interleukin-8 by SARS-CoV-2 Spike protein is inhibited in bronchial epithelial IB3–1 cells by a miR-93-5p agomiR, Int Immunopharmacol 101 (Pt B) (2021), 108201.
[46] A. Majumder, J.E. Straub, Addressing the excessive aggregation of membrane proteins in the MARTINI model, J Chem Theory Comput 17 (4) (2021) 2513–2521.
[47] H. Woo, S.J. Park, Y.K. Choi, T. Park, M. Tanveer, Y. Cao, N.R. Kern, J. Lee, M. S. Yeom, T.I. Croll, C. Seok, W. Im, Developing a fully glycosylated full-length SARS-CoV-2 spike protein model in a viral membrane, J. Phys. Chem. B 124 (33) (2020) 7128–7137.
[48] D. Branduardi, G. Bussi, M. Parrinello, Metadynamics with adaptive Gaussians, J Chem Theory Comput 8 (7) (2012) 2247–2254.
[49] J.S. Hub, M.B. Kubitzki, B.L. de Groot, Spontaneous quaternary and tertiary T-R transitions of human hemoglobin in molecular dynamics simulation, PLoS Comput. Biol. 6 (5) (2010), e1000774.
[50] S. Khan, M.S. Shafiei, C. Longoria, J.W. Schoggins, R.C. Savani, H. Zaki, SARS-CoV-2 spike protein induces inflammation via TLR2-dependent activation of the NF-κB pathway, Elife 10 (2021).
[51] A.B. Poma, M. Cieplak, P.E. Theodorakis, Combining the MARTINI and structure-based coarse-grained approaches for the molecular dynamics studies of conformational transitions in proteins, J Chem Theory Comput 13 (3) (2017) 1366–1374.
[52] W.Y. Chi, Y.D. Li, H.C. Huang, T.E.H. Chan, S.Y. Chow, J.H. Su, L. Ferrall, C. F. Hung, T.C. Wu, COVID-19 vaccine update: vaccine effectiveness, SARS-CoV-2 variants, boosters, adverse effects, and immune correlates of protection, J. Biomed. Sci. 29 (1) (2022) 82.